

Oh Boi Its my Thesis

by

Anna Maria Houk

A thesis
presented to the University of Waterloo
in fulfillment of the
thesis requirement for the degree of
Masters of Science
in
Electrical and Computer Engineering - Quantum Information

Waterloo, Ontario, Canada, 2022

© 2022

Author's Declaration

I hereby declare that I am the sole author of this thesis. This is a true copy of the thesis, including any required final revisions, as accepted by my examiners.

I understand that my thesis may be made electronically available to the public.

Abstract

This is the abstract.

Acknowledgements

.

Dedication

.

Table of Contents

List of Figures	viii
List of Tables	x
1 Introduction	1
1.1 Motivation	1
1.2 Thesis Outline	1
2 Background	2
2.1 Hollow-Core Photonic Crystal Fiber	2
2.1.1 Conventional TIR Guidance	2
2.1.2 Photonic Crystal Bandgap	2
2.1.3 Bandgap Shift	5
2.1.4 Mode Distribution	6
2.2 Carbon Nanotubes	9
2.2.1 Characterizing Carbon Nanotubes	10
2.2.2 Nonlinear Optical Properties of CNTs	15
2.2.3 Fluorescence of CNTs	16
3 Liquid-Filled HCPCF	21
3.1 Filling Methods	21

3.2	Experimental Set-Up	23
3.3	H ₂ O and D ₂ O Transmission	23
3.4	Results	25
3.4.1	Selective Filling	25
3.4.2	Full-Fiber Filling	27
4	Fluorescence Tests	29
4.1	Bandgap Overlap	29
4.2	Indocyanine Green	32
4.3	Background	32
4.3.1	Absorption	32
4.3.2	Fluorescence	34
4.3.3	Photostability	35
4.4	Experiment Set-Up	37
4.5	Results	38
5	Future Work	39
5.1	ECDL	39
	References	40
	APPENDICES	41
A	PDF Plots From Matlab	42
A.1	Derivation of the 1D Propagation Matrix	42
	Glossary	45
	Abbreviations	46
	Nomenclature	47
	List of Symbols	48

List of Figures

2.1	Many figures	3
2.2	REPLACE Chiralities of CNTs with red dots indicating metallic and open dots [1].	11
2.3	REPLACE Bands for (a)(c)Metallic and (b)(d)Semiconducting CNTs and their energy band gaps [3]	12
2.4	Chiralities of CNTs with red dots indicating metallic and open dots Calculated gap energies between mirror-image spikes in density of states for $\gamma = 2.75$ eV. For (solid circles) metallic and (open circles) semiconducting, and (double circles) armchair CNTs. [6].	14
2.5	Group characteristics of CNTs colored by (a)chiral angle and (b)diameter	18
3.1	Side profile of collapsed cladding 1550HC fiber running the fiber splicer with varying current strength and duration.	22
3.2	Variation between fibers using splicer settings 70ms 25ms	22
3.3	Fiber transmission experimental set-up.	23
3.4	The transmission of heavy water(green) and regular water(blue) is shown for slabs of thickness ranging from 1cm to 8cm in increments of 1cm using absorption data recorded by [4].	24
3.5	Transmission of H ₂ O and D ₂ O in (a)selectively-filled 800nm hollow-core fiber.	26
3.6	Modeshape of 1550 hollow-core fiber filled with (a)air (b)heavy water (c)distilled water. Fiber filled with heavy water maintains a Gaussian profile while the fiber with regular distilled water shows some distortion.	27
3.7	Transmission of H ₂ O and D ₂ O in fully-filled 1550nm hollow-core fiber. . . .	27

4.1	Hollow-core fiber bandgap overlayed on CNT emission vs. excitation wavelengths	30
4.2	1550HC CNTs	31
4.3	Absorption cross-section at peak wavelengths 700nm(blue) and 780nm(green) for ICG dissolved in D2O(a) and H2O(b) . Data from (cite) was fitted using a linear regression model.	33
A.1	Schematic of quarter wavelength stack	42

List of Tables

4.1	Thorlabs fiber bandgap shift.	29
4.2	CNTs with emission and excitation transmittable through HC1550 filled with D ₂ O.	31
4.3	Absorption Cross Section parameter fitting of ICG dissolved in deionized water. Fitting done with linear regression on σ vs. concentration data measured at $\lambda = 780nm$ from literature.	34
4.4	Absorption Cross Section parameter fitting of ICG dissolved in deionized water. Fitting done with linear regression on σ vs. concentration data at $\lambda = 700nm$ from literature.	34
4.5	Absorption Cross Section parameter fitting of ICG dissolved in heavy water. Fitting done with linear regression on σ vs. concentration data at $\lambda = 700nm$ from literature.	34

Chapter 1

Introduction

In the beginning, there was π :

$$e^{\pi i} + 1 = 0 \tag{1.1}$$

A [computer](#) could compute π all day long. In fact, subsets of digits of π 's decimal approximation would make a good source for psuedo-random vectors, [v](#) .

1.1 Motivation

See equation [1.1](#) on page [1](#).¹

1.2 Thesis Outline

The credo of the [American Association of Amateur Astronomers and Zoologists \(AAAAZ\)](#) was, for several years, several paragraphs of gibberish, until the [dingledorf](#) responsible for the [AAAAZ](#) Web site realized his mistake:

¹A famous equation.

Chapter 2

Background

2.1 Hollow-Core Photonic Crystal Fiber

2.1.1 Conventional TIR Guidance

2.1.2 Photonic Crystal Bandgap

The 1D and 2D views of the structure

A periodic non-magnetic medium will have repeating dielectric constant

$$\varepsilon(\mathbf{r}) = \varepsilon(\mathbf{r} + \mathbf{a}) \quad (2.1)$$

Due to its discrete and invariant translation symmetry, the dielectric constant along the medium can be expanded as a Fourier series

$$\varepsilon(\mathbf{r}) = \sum_{\mathbf{G}} \varepsilon_{\mathbf{G}} e^{i\mathbf{G} \cdot \mathbf{r}} \quad (2.2)$$

Where \mathbf{G} are the reciprocal lattice vectors such that $\mathbf{G} \cdot \mathbf{a} = 2\pi n$. Expressing the electric field also as a Fourier integral

$$\mathbf{E}(\mathbf{r}) = \iiint d^3\mathbf{k} \mathbf{A}(\mathbf{k}) e^{i\mathbf{k} \cdot \mathbf{r}} \quad (2.3)$$

Using the Maxwell equations defined in - the wave equation can be written in terms of the electric field

$$\nabla \times (\nabla \times \mathbf{E}) - \omega^2 \varepsilon(\mathbf{r}) \mu_0 \mathbf{E} = 0 \quad (2.4)$$

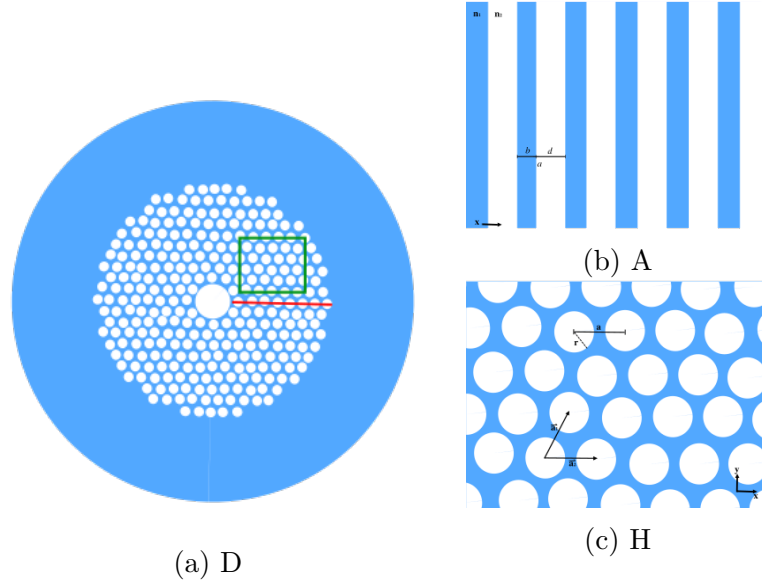


Figure 2.1: Many figures

Substituting (2.2) and (2.3) into the above results in the dispersion relation:

$$\mathbf{k} \times (\mathbf{k} \times \mathbf{A}(\mathbf{k})) + \omega^2 \mu_0 \sum_{\mathbf{G}} \varepsilon_{\mathbf{G}} \mathbf{A}(\mathbf{k} - \mathbf{G}) = 0 \quad (2.5)$$

in where for any vector \mathbf{K} the solutions of (2.5) for the coefficient $\mathbf{A}(\mathbf{K})$ are grouped with the coefficients $\mathbf{A}(\mathbf{K} - \mathbf{G})$, decoupling the coefficients of other vectors that cannot be expressed in the form $\mathbf{K} - \mathbf{G}$. Disregarding the decoupled vectors, the total electric field can be described as a superposition of normal modes with regard to a chosen vector \mathbf{K} :

$$\mathbf{E}_{\mathbf{k}}(\mathbf{r}) = \sum_{\mathbf{G}} \mathbf{A}(\mathbf{K} - \mathbf{G}) e^{i(\mathbf{k} - \mathbf{G}) \cdot \mathbf{r}} \quad (2.6)$$

With a little algebra, we can pull out the Bloch theorem for the electric field from (2.6)

$$\mathbf{E}_{\mathbf{k}}(\mathbf{r} + \mathbf{a}) = e^{i\mathbf{k} \cdot \mathbf{a}} \mathbf{E}_{\mathbf{k}}(\mathbf{r}) \quad (2.7)$$

(Expand) Returning to (2.5), can fix ω to find the corresponding \mathbf{K} and normal modes of the system. However, in the case of photonic crystals there are ranges of frequencies that have no \mathbf{K} s with real solutions, which implies that waves of these frequencies cannot propagate through the photonic crystal. These non-propagating frequencies are referred to as the photonic band gap.

1D Photonic Bandgap

Returning to the 1D periodic stack pictured in A.1 the periodicity of dielectric constant is described by $\varepsilon(z) = \varepsilon(z + p)$ where $p = b + a$, the length of one period. The reciprocal lattice vector will be $\mathbf{G}_n = n \frac{2\pi}{p} \hat{z}$ and plugging into the Fourier series expansion of $\varepsilon(z)$ from (2.2)

$$\varepsilon(z) = \sum_{n=-\infty}^{\infty} \varepsilon_n e^{in \frac{2\pi}{p} z} \quad (2.8)$$

From the reduction to propagation in the z-direction with the electric field oriented in x-direction, (2.5) simplifies

$$K^2 A(K) + \omega^2 \mu_0 \sum_{n=-\infty}^{\infty} \varepsilon_n A(K - n \frac{2\pi}{p}) = 0 \quad (2.9)$$

Expanding the Fourier coefficients to the 1st order and reducing the equations to the dominant coefficients of the form $A(K)$ and $A(K - \frac{2\pi}{p})$. $|K - g| = K$ and $K = \frac{\pi}{p}$ gives a system of equations that can be solved to find the dispersion relation $\omega(K)$.

$$\begin{cases} (K^2 - \omega^2 \mu_0 \varepsilon_{00}) A(K) = \omega^2 \mu_0 \varepsilon_1 A(K - g) \\ \omega^2 \mu_0 \varepsilon_{-1} A(K) = ((K - g)^2 - \omega^2 \mu_0 \varepsilon_{00}) A(K - g) \end{cases} \quad (2.10)$$

The equations relating these two modes has a solution at

$$(K^2 - \omega^2 \mu_0 \varepsilon_{00}) ((K - g)^2 - \omega^2 \mu_0 \varepsilon_{00}) - (\omega^2 \mu_0 \varepsilon_1) (\omega^2 \mu_0 \varepsilon_{-1}) = 0 \quad (2.11)$$

noting $\varepsilon_1 = \varepsilon_{-1}^*$ and $K \approx 2g$ simplifies the relationship

$$(K^2 - \omega^2 \mu_0 \varepsilon_{00})^2 - (\omega^2 \mu_0 |\varepsilon_1|^2)^2 = 0 \quad (2.12)$$

$$\omega_{\pm}^2 = \frac{K^2}{\mu_0 (\varepsilon_{00} \mp |\varepsilon_1|)} \quad (2.13)$$

The dispersion relation has two possible solutions, which specify the top and bottom of the photonic bandgap edges, as illustrated in Fig.- [fig of omega v. K] If the solving for the wavevector at a frequency between ω_{\pm} , only complex solutions will exist. This means that only evanescent waves, not electromagnetic waves, propagate through the medium while the electromagnetic waves are reflected back; the medium acts as a mirror for the bandgap wavelengths.

This is the the phenomena that allows for HCPCF to guide certain frequencies of light - wavelengths in the bandgap are reflected by surrounding Bragg Grating confining them to the core of the fiber, while the rest are allowed to propagate through the grating.

2D Photonic Bandgap

To understand the full picture of light propagation in hollow-core fiber, we need to expand to the 2D case pictured in 2.1.c primitive lattice vectors

$$\mathbf{a}_1 = a\hat{x} \quad \mathbf{a}_2 = \frac{a}{2}\hat{x} + \frac{a\sqrt{3}}{2}\hat{y} \quad (2.14)$$

primitive reciprocal lattice vectors $\mathbf{b} \cdot \mathbf{a} = 2\pi\delta_{ij}$

$$\mathbf{b}_1 = \frac{2\pi}{a}\hat{x} - \frac{2\pi}{a\sqrt{3}}\hat{y} \quad \mathbf{b}_2 = \frac{4\pi}{a\sqrt{3}}\hat{y} \quad (2.15)$$

The reciprocal lattice vector will be $\mathbf{G} = n\mathbf{b}_1 + m\mathbf{b}_2$ where n, m are scaling factors. Taking propagation in the xy-plane ($K_z = 0$ and $z = 0$ for simplicity), $\mathbf{K} = K_x\hat{x} + K_y\hat{y}$ and $\mathbf{r} = x\hat{x} + y\hat{y}$. The "In the previous two sections, we used the field patterns as our guide to understand which aspects of two-dimensional photonic crystals lead to TM and TE band gaps. By combining our observations, we can design a photonic crystal that has band gaps for both polarizations. Jovanopolous"

"reciprocal lattice that is also hexagonal, but rotated relative to the original lattice by 30deg. The first Brillouin zone is defined by plotting perpendicular bisectors to the reciprocal lattice vectors. The irreducible Brillouin zone is 1/12 of the first Brillouin zone; because of the lattice symmetry, it is sufficient to only solve the Bloch modes inside this irreducible Brillouin zone. Moreover, in order to determine the photonic band gap, it is sufficient to solve the band diagram only along the edges of the green triangle. Lukin"

This region is a simple triangle with side lengths $\Gamma X = \frac{2\pi}{a\sqrt{3}}$, $\Gamma J = \frac{4\pi}{3a}$, $\Gamma J = \frac{2\pi}{3a}$

2.1.3 Bandgap Shift

modal magnetic field distributions satisfy:

$$(\nabla_t^2 + k^2 n(\mathbf{r})^2 - \beta) \mathbf{H}(\mathbf{r}) = (\nabla_t \times \mathbf{H}(\mathbf{r})) \times (\nabla_t \ln(n(\mathbf{r})^2)) \quad (2.16)$$

gives scaling law for absolute refractive index at fixed contrast "a solution for a transverse scale represented by Λ is replicated in an identical structure with a different Λ if the wavelength is scaled proportionately, to keep $k\Lambda$ constant" Scaling law for the wave equation for the transverse coordinates $X = x\Lambda^{-1}$ $Y = y\Lambda^{-1}$ where Λ is a solution to the transverse scale.

$$n(X, Y) = \begin{cases} 1, & n_1 \text{ (high RI)} \\ 0, & n_2 \text{ (low RI)} \end{cases} \quad (2.17)$$

normalized scaled wave equation:

$$\nabla_{\perp}^2 \Psi + (v^2 n(X, Y) - w^2) \Psi = 0 \quad (2.18)$$

With $\nabla_{\perp} = \partial^2/\partial X^2 + \partial^2/\partial Y^2$ solving for the frequency parameter v^2 and eigenvalue w^2 :

$$\begin{aligned} v^2 &= \Lambda^2 k^2 (n_1^2 - n_2^2) \\ w^2 &= \Lambda^2 (\beta^2 - k^2 n_2^2) \end{aligned} \quad (2.19)$$

from the equation above we see that the w^2 is determined by the frequency parameter v^2 and the index distribution function $n(X, Y)$. This implies that w^2 and v^2 are invariant with changes to the parameters k, Λ, n_1, n_2 . $k = \omega/c$ $\beta = k \cos \theta$ longitudinal component of the wavevector. Because the light propagates along the fiber, much of its wavevector is taken up by the longitudinal component.

In the HCPCF case where the glass refractive index is held constant and the air in the fiber is replaced by a new material the equations can be rewritten with $n_1 = n_{glass}$ and $n_2 = n_{air} = 1$:

$$\begin{aligned} v^2 - w^2 &= \Lambda^2 (k^2 n_{glass} - \beta^2) \\ v &= k \Lambda n_{glass} \sqrt{n_{air} - \frac{n_{air}}{n_{new}}} \end{aligned} \quad (2.20)$$

The initial index contrast $N_0 = \frac{n_{air}}{n_{glass}}$ moves to $N = \frac{n_{new}}{n_{glass}}$ with the change in RI $n_{air} < n_{new} < n_{glass}$. This leads to the new center bandgap to be governed by the equation:

$$\lambda = \lambda_0 \sqrt{\frac{1 - N^{-2}}{1 - N_0^{-2}}} \quad (2.21)$$

"We emphasise that the scalar wave equation (and therefore the scaling laws derived from it) is accurate for the smallest index contrasts only. However, for step-index structures the vector term in Eq. (2) only exists at boundaries, so the scalar wave equation accurately represents wave propagation elsewhere. Since bandgaps arise from interference and resonance effects among such generic waves, the scaling laws of Eq. (5) should be at least approximately valid" 1.45 RI contrast

2.1.4 Mode Distribution

a) For a two-level atom, the coupling constant – g – [Eq. 2.6] scales inversely to this 'effective mode area' [Eq. before 2.1] (in the interaction energy term between atom and

the field). mode is like a Gaussian [given by the mode function $f(x,y)$] the photon interacts more strongly if the atom is placed in the center of the mode.)

effective mode area:

$$A = \frac{\int dx dy |f_k(x,y)|^2}{|f_k(x_a, y_a)|^2} \quad (2.22)$$

where $f_k(x,y)$ is the transverse mode function and (x_a, y_a) is the position of the atom, is approximately constant in the range of the relevant longitudinal wave numbers

coupling constant:

$$g_\omega = \sqrt{\frac{\omega}{4\pi\epsilon\hbar c A}} d_{eg} \quad (2.23)$$

(2.5) dipole interaction Hamiltonian

b) Apparently, this coupling constant term tells us parameters such as:

i) how likely it is for an excitation in the emitter is released into the waveguide mode γ_{1D} , versus free-space γ_0 . [3]

$$\gamma_{1D} = 2\pi g_{\omega_A}^2 = \frac{\sigma_A}{2A} \gamma_0 \quad (2.24)$$

”where the second expression directly exhibits the scaling with the transverse extension of the waveguide. It is related to the atomic radiative cross section $\sigma_A = \frac{3\lambda^2}{2\pi}$. A natural lower bound on the transverse mode size is at about $A \sim (\frac{\lambda}{2})^2$. (lowest-order mode in hollow metallic wave- guide), implying a maximum achievable coupling ratio $\gamma_{1D}/\gamma_0 \sim 1$. In the range $\sigma_A \sim A$, one has a strong waveguide-atom coupling, which is manifested by the fact that the atom dissipates its energy equally into the waveguide and the free-space “lossy” modes.” [1]

ii) optical depth (OD) for a single atom is (about) the ratio of $(\gamma_{1D})/(\gamma_0)$ or the ratio of the cross-section area of the atom to that of the effective mode-area.

$$OD = \frac{\sigma_A}{\sigma_M} = \frac{\gamma_{1D}}{\gamma_0} \quad (2.25)$$

c) OPTICAL DEPTH CALCULATIONS: Optical depth (OD) tells about how opaque the system is. Transmitted intensity goes by $T = \exp(-OD)$. Normally, N emitters might scale linearly to give an optical depth $N * OD$. But now (due to its position) each emitter might have its own mode area.

Examples of taking this into account (with maybe slightly different conventions) for atoms are mentioned in these two references[4, 5]:

$$OD_{fiber} = \int_0^L \int_0^r n(\rho, z) OD 2\pi \rho d\rho dL \quad (2.26)$$

r and L represent the radius and length of the ensemble, which in the case of solution-filled HCPCF is the radius and length of the fiber. This assumes that the particulates outside of the core do not have a significant contribution. If the distribution of molecules is take to be uniform along the fiber length and radius of the core, then the number density will be:

$$n(\rho, z) = \begin{cases} 0, & |z| > L/2 \\ (1/L)(1/\rho), & |z| < L/2 \end{cases} \quad (2.27)$$

Bibliography

- [1] P. Domokos, P. Horak, and H. Ritsch, “Quantum description of light-pulse scattering on a single atom in waveguides,” *Phys. Rev. A*, vol. 65, no. 3, p. 033832, Mar. 2002, doi: 10.1103/PhysRevA.65.033832.
- [2] P. Solano et al., “Optical Nanofibers: a new platform for quantum optics,” vol. 66, 2017, pp. 439–505. doi: 10.1016/bs.aamop.2017.02.003.
- [3] M. T. Manzoni, “New Systems for Quantum Nonlinear Optics,”. 2017, Thesis, p. 39-40.
- [4] M. Bajcsy et al., “Laser-cooled atoms inside a hollow-core photonic-crystal fiber,” *Phys. Rev. A*, vol. 83, no. 6, p. 063830, Jun. 2011, doi: 10.1103/PhysRevA.83.063830.
- [5] A. P. Hilton, C. Perrella, F. Benabid, B. M. Sparkes, A. N. Luiten, and P. S. Light, “High-efficiency cold-atom transport into a waveguide trap,” *Phys. Rev. Applied*, vol. 10, no. 4, p. 044034, Oct. 2018, doi: 10.1103/PhysRevApplied.10.044034. A

2.2 Carbon Nanotubes

First discovered by S.Iijima and T. Ichihashi in 1993, carbon nanotubes (CNT) are single layers of graphene rolled up into a hollow cylinder near 1 nm in diameter and near 1μm in length. While graphene is a 2-dimensional material, the dimensions of CNTs allow them to be treated as 1-dimensional materials.

2.2.1 Characterizing Carbon Nanotubes

The main descriptive properties of CNTs are the chiral vector, which is a scaled integer-valued combination of the unit vectors for the honeycomb structure of graphene, written in the form (n, m) .

$$C_h = na_1 + ma_2 = (n, m) \quad (2.28)$$

The unit vectors in Cartesian coordinates are

$$a_1 = \left(\frac{\sqrt{3}}{2}, \frac{1}{2}\right)\sqrt{3}a_{C-C} \quad a_2 = \left(\frac{\sqrt{3}}{2}, -\frac{1}{2}\right)\sqrt{3}a_{C-C} \quad (2.29)$$

and have equal length a_{C-C} , where a_{C-C} is the length of the carbon bond, which for graphene is 1.421 (Å), and often approximated as 1.44(Å) for CNTs, though there is variation depending on the curvature of the nanotubes[4]. The chiral vector is of high value as it reveals a lot of information about the electronic and optical properties of individual CNTs. The chiral angle, the angle between the unit vectors, gives the direction of the chiral vector and is defined as

$$\theta = \tan^{-1} \left[\frac{m\sqrt{3}}{m + 2n} \right] \quad (2.30)$$

and the diameter of a nanotube as

$$d_t = \frac{a_{C-C}\sqrt{3}}{\pi} \sqrt{n^2 + nm + m^2} \quad (2.31)$$

Due to the geometry of graphene, CNTs have a six-fold rotational symmetry and the connection points of the lattice, i.e. the way that the graphene is rolled into a tube will produce equivalent CNTs between θ and $\theta + 60^\circ$, thus the tube geometries are often constrained to the first range. Nanotubes with a chiral angle of 0° are called zigzag tubes and chiral angles of $\pm 30^\circ$ are called armchair tubes due to the pattern made by their circumference as shown in the Figure 2, and are the two configurations in which CNTs are anti chiral, meaning that their structures are indistinguishable from their mirrored image, while all in between-angled nanotubes are chiral, i.e. distinguishable from their mirrored image. The diameter and angle actually vary the electronic band structure of the CNT significantly. CNTs have an additional electron confinement around their circumference[3] and as can be seen from the above definitions, the tube diameter of CNTs is quantized and varies depending on how the graphene honeycomb lattice is cut, will also follow the boundary condition

$$C_h \cdot \kappa = 2\pi q \quad (2.32)$$

where is the cutting line along graphene and q is an integer number. Depending on where graphene energy bands are along the cutting line, the corresponding CNT will become metallic or a semiconductor. In Figure 1, the metallic and semiconducting CNTs are mapped out, and a pattern emerges with CNTs with their chiralities $m-n$ being a multiple of 3 emerging as metals. Single CNTs exhibit polarization dependence with the electric field in optical selection rules, i.e. the possible transitions from one quantum state to another [5]. The polarization dependence is only strong in zigzag type nanotubes however. The dipole operator in anti chiral tubes will have a parity of -1 in the horizontal plane dipole operator along the z-axis and a +1 parity for dipole vectors along the x, y plane. For z polarized light there is no electronic band transition, while for light polarized perpendicular to the z axis, the angular momentum quantum number can shift by 1. Thus, CNTs will absorb light with the optical polarization parallel to the axial direction of the tube, but in a bundle or grouping of random-oriented CNTs, there will be no polarization dependence.

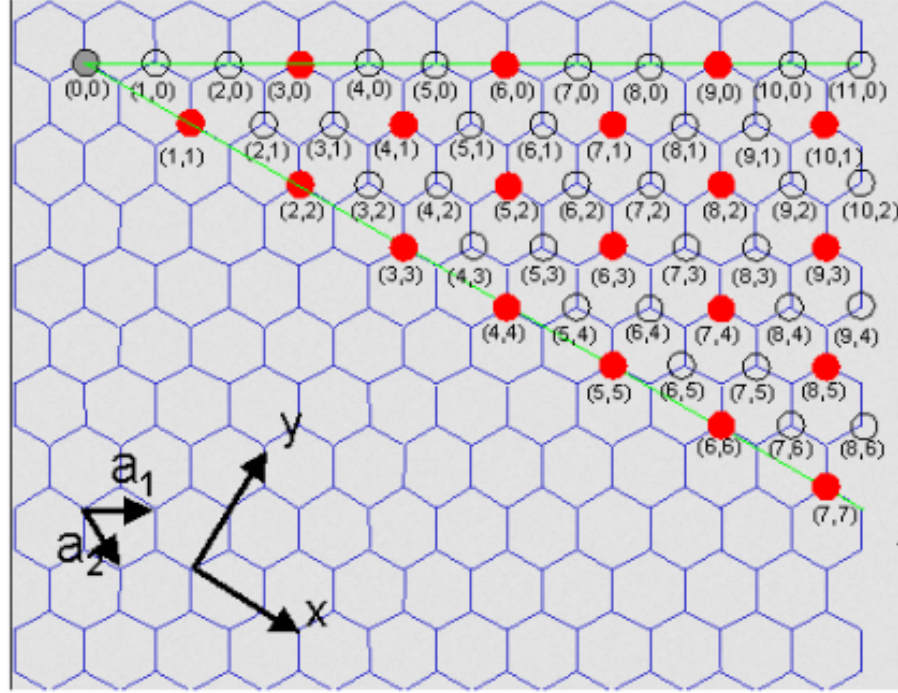


Figure 2.2: REPLACE Chiralities of CNTs with red dots indicating metallic and open dots [1].

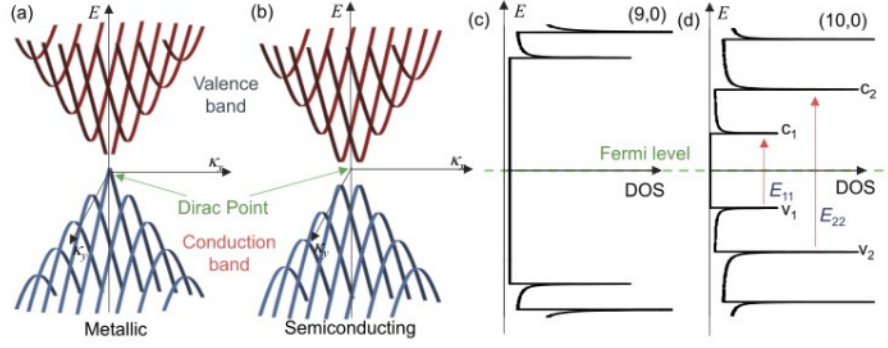


Figure 2.3: REPLACE Bands for (a)(c)Metallic and (b)(d)Semiconducting CNTs and their energy band gaps [3]

In the same year as the emergence of CNTs as a unique material, H. Kataura measured the optical absorption spectra of CNTs of various diameter CNTs performing photothermal deflection spectroscopy, which measures heat produced during relaxation of the electron hole pair generated by the absorbed light [6], an example of the optical absorption spectra are shown in Figure 4. While the absorption spectra across various CNT samples were consistent, the peak positions varied. Using the energy dispersion relations for pi-bands of the graphite [6]

$$E_{2D} = \pm \gamma \sqrt{1 + 4\cos(\frac{\sqrt{3}k_x a}{2})\cos(\frac{k_y}{2}) + 4\cos^2(\frac{k_y}{2})} \quad (2.33)$$

where γ is the overall integration and k_x, k_y are the reciprocal lattice vectors, fulfilling the periodic boundary condition for chiral vectors from Eq. (5), the one-dimensional energy band of CNTs could be calculated. Referring to Figure 3, the spikes in the DOS correspond to the energy levels of the optical transitions. Plotting the Gap energies from this model against the nanotube diameter in Figure 5, referred to commonly as a Kataura plot, shows how the first transition energy of CNTs has a relationship to the diameter by

$$E_{11} = \frac{2\gamma a_{C-C}}{d} \quad (2.34)$$

and the average band gap energies split along semiconductor and metallic chiral values. In short the absorption peak wavelength of a nanotube sample is determined by the mean tube diameter, and the absorption spectral bandwidth will be determined by the tube diameter distribution of the CNT sample.

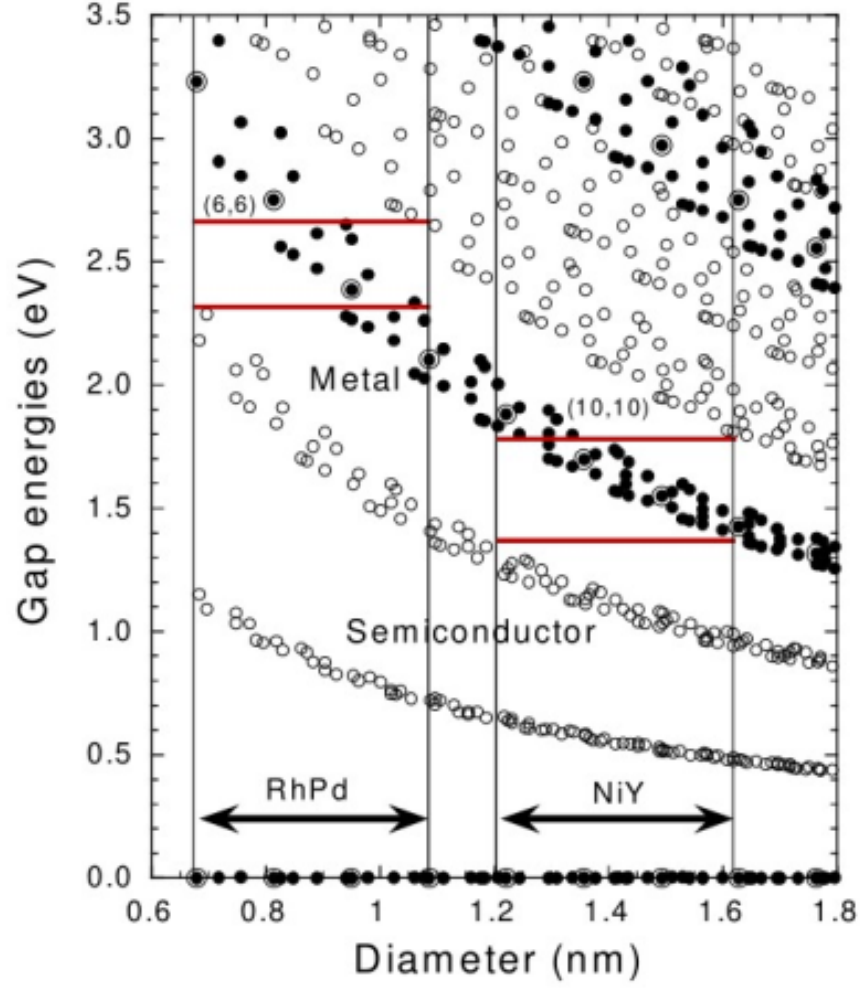


Figure 2.4: Chiralities of CNTs with red dots indicating metallic and open dots Calculated gap energies between mirror-image spikes in density of states for $\gamma = 2.75$ eV. For (solid circles) metallic and (open circles) semiconducting, and (double circles) armchair CNTs. [6].

2.2.2 Nonlinear Optical Properties of CNTs

The general relationship between the polarization and electric field of a material is defined [7] as

$$P(t) = \epsilon_0(\chi^{(1)}E(t) + \chi^{(2)}E^2(t) + \chi^{(3)}E^3(t) + \dots) \quad (2.35)$$

where $\chi^{(1)}$ is the linear susceptibility and $\chi^{(2)}$ and $\chi^{(3)}$ are the second and third order susceptibility. Due to the inversion symmetry of the CNT's structure, the second-order susceptibility is zero. However, a large third-order nonlinearity in CNTs has been measured [12] and is theorized to be a product of the one dimensional motion of the delocalized π -band electrons at a fixed lattice ion configuration [13]. The third-order nonlinearity is responsible for the saturable absorption of a material as well as the nonlinear Kerr effect. The refractive index as defined in Eq.(9) is composed of the real part of the third-order susceptibility with I defining the optical intensity and ω as the optical angular frequency, and is the nonlinear refractive index.

$$n = n_0 + n_2I = n_0 + \frac{3\text{Re}[\chi^{(3)}]}{4\epsilon_0cn_0^2}I \quad (2.36)$$

The absorption coefficient defined by Eq.(10) is composed of the imaginary part of the third-order susceptibility and α_0 , and α_{int} are the linear absorption coefficient, the non saturable absorption coefficient, and refractive index respectively.

$$\alpha = \frac{\alpha_0}{1 + \frac{I}{I_S}} + \alpha_{int} \sim \alpha_0 + \alpha_{int} + \frac{3\omega\text{Im}[\chi^{(3)}]}{2\epsilon_0c^2n_0^2}I \quad (2.37)$$

The saturation intensity, I_S , is the power per unit area it takes in a steady state to reduce the absorption to 1/2 the unbleached (or completely saturated) value and can be written in terms of

$$I_S = \frac{hf}{\sigma\tau} = \frac{E_S}{\tau} \quad (2.38)$$

where σ is the absorption cross section and E_S is the saturation fluence, which is the fluence (i.e. energy per unit area) it takes to reduce the initial fluence value to e^{-1} and τ is the recovery time of the material.

The saturable absorption, as defined by Eq.(11), is a phenomenon where high intensity light will reduce the absorption of a material, but at weak intensity, the light will be absorbed and cause attenuation. This property of materials with strong third-order susceptibility like CNTs can be used to filter out weaker optical signals in noisy optical pulses, while simultaneously allowing strong pulses to pass through. Saturable absorption is observed in all materials with optical absorption resulting from electron transition

between two energy levels [5], but it is rare to find materials that have a recovery time that has a fast recovery time compared to the pulse duration, which in ultra-fast laser applications is in the few picosecond to femtosecond range. The ultra-fast response time of CNTs is only true however for bundles of CNTs with variations in their diameter due to entanglement between semiconducting and metallic via electrons tunneling and coupling from semiconducting CNTs to metallic CNTs [8].

2.2.3 Fluorescence of CNTs

The first Van Hove optical transition (E11) corresponds to the emission frequency and the second Van Hove optical transition (E22) corresponds to the excitation frequency. Equations for first and second van Hoven Transitions optical transition wavelengths as a function of diameter in nanometers and chiral angle are degrees derived in [10], but parameters from [9], which were found by fitting to data of samples of individual SWNT in aqueous sodium dodecyl sulfate (SDS) suspension and are valid for CNT diameters greater than 0.5nm. The parameters differ for each CNT “group”, i.e $(n-m) \bmod 3 = 1$ is group 1 $(n-m) \bmod 3 = 2$ is group 2 $(n-m) \bmod 3 = 0$ are metallic CNTs and do not fluoresce.

Though it is unknown what specific effects contribute to the fitted parameters with the particular samples used, [9]found that other aqueous solutions have comparative spectral shifts of less than 2% compared to the equations when compared to other published results. Comparing to an experimental PL map using a different solutio[11], the equation results match quite well (the CNTs present in the left sample are marked in red on the right plot). We can see the expected variation from different solutions, for example CNT (10, 8) has a slightly higher excitation wavelength and slightly lower emission wavelength in SDS than in the NaDDBS/D2O solutions.

Only fully intact and individually dispersed semiconducting CNTs emit fluorescence CNTs coatings or placed on a substrate don’t really fluoresce Interactions between CNTs typically cause quenching effects Though certain materials/solvents (varies with each CNT) can increase fluorescence Isolation is one of the largest factors in quantum yield Only in semiconductor-type CNTs

Desired type of CNTs can be targeted and isolated in a single step using modified aqueous two-phase extraction(ATPS). Hydration modulating agents are mixed in to tune the arrangement of surfactants on their surface

Depending on the mixture, selected CNTs turn highly hydrophobic or hydrophilic

Spectral shift due to the change in the local dielectric environment surrounding CNTs created by solvents and adsorbed molecules.[14]

$$(Emission)\lambda_{11} = \left[\frac{1e7(cm^{-1})}{157.5 + 1066.9d_t} - 771(cm^{-1}) \frac{\cos(3\theta)^{1.374}}{d_t^{2.272}} \right]^{-1} \quad (2.39)$$

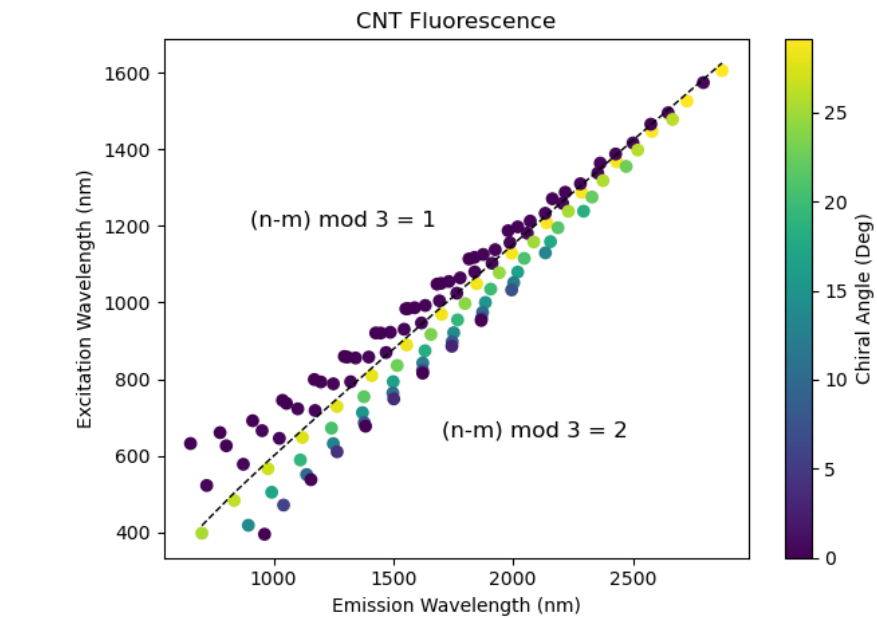
$$(Excitation)\lambda_{22} = \left[\frac{1e7(cm^{-1})}{145.6 + 575.7d_t} + 1326(cm^{-1}) \frac{\cos(3\theta)^{0.828}}{d_t^{1.809}} \right]^{-1} \quad (2.40)$$

$$(Emission)\lambda_{11} = \left[\frac{1e7(cm^{-1})}{157.5 + 1066.9d_t} + 347(cm^{-1}) \frac{\cos(3\theta)^{0.886}}{d_t^{2.129}} \right]^{-1} \quad (2.41)$$

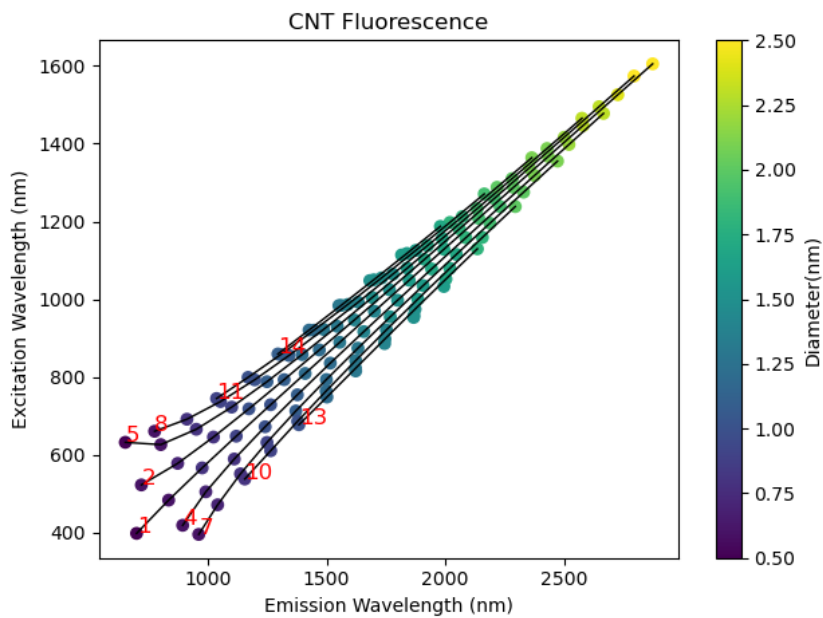
$$(Excitation)\lambda_{22} = \left[\frac{1e7(cm^{-1})}{145.6 + 575.7d_t} - 1421(cm^{-1}) \frac{\cos(3\theta)^{1.110}}{d_t^{2.497}} \right]^{-1} \quad (2.42)$$

Group 1 v. Group 2 Group 1 CNTs have lower Stokes shifts than Group 2 Group 1 have small chiral angles (i 2o) Group 2 span full 0o to 30o chiral angle range, but are grouped along chiral number difference (n - m)

Excitation/Emission wavelengths Increase in Stokes shifts with diameter along chiral difference (n - m) lines Noted in red on lower plot, connected by black lines Increase in ex/em wavelengths with diameter



(a)



(b)

Figure 2.5: Group characteristics of CNTs colored by (a)chiral angle and (b)diameter

Bibliography

- [1] S. Dresselhaus, “PHYSICS OF CARBON NANOTUBES,” Carbon, 33(7), 883-891, 1995.
- [2] V. Popov, “Carbon nanotubes: properties and application,” Materials Science and Engineering: R: Reports, vol. 43, no. 3, pp. 61–102, Jan. 2004.
- [3] S. Yamashita, “Nonlinear optics in carbon nanotube, graphene, and related 2D materials,” APL Photonics, vol. 4, no. 3, p. 034301, Mar. 2019.
- [4] R. Saito, M. Fujita, G. Dresselhaus, and M. S. Dresselhaus, “Electronic structure of chiral graphene tubules,” Appl. Phys. Lett., vol. 60, no. 18, pp. 2204–2206, May 1992.
- [5] C. Thomsen, S. Reich, and J. Maultzsch, Carbon Nanotubes: Basic Concepts and Physical Properties, 1st ed. Wiley, 2004.
- [6] H. Kataura et al., “Optical properties of single-wall carbon nanotubes,” Synthetic Metals, vol. 103, no. 1–3, pp. 2555–2558, Jun. 1999.
- [7] S. Yamashita, “A Tutorial on Nonlinear Photonic Applications of Carbon Nanotube and Graphene,” J. Lightwave Technol., vol. 30, no. 4, pp. 427–447, Feb. 2012.
- [8] A. Gambetta et al., “Sub-100 fs two-color pump-probe spectroscopy of Single Wall Carbon Nanotubes with a 100 MHz Er-fiber laser system,” p. 8, 2008.
- [9] R. B. Weisman and S. M. Bachilo, “Dependence of Optical Transition Energies on Structure for Single-Walled Carbon Nanotubes in Aqueous Suspension: An Empirical Kataura Plot,” Nano Lett., vol. 3, no. 9, pp. 1235–1238, Sep. 2003.

- [10] S. M. Bachilo, M. S. Strano, C. Kittrell, R. H. Hauge, R. E. Smalley, and R. B. Weisman, “Structure-Assigned Optical Spectra of Single-Walled Carbon Nanotubes,” *Science*, vol. 298, no. 5602, pp. 2361–2366, Dec. 2002.
- [11] S. Giordani et al., “Debundling of Single-Walled Nanotubes by Dilution: Observation of Large Populations of Individual Nanotubes in Amide Solvent Dispersions,” *J. Phys. Chem. B*, vol. 110, no. 32, pp. 15708–15718, Aug. 2006.
- [12] A. Martinez and S. Yamashita, “Carbon Nanotube-Based Photonic Devices: Applications in Nonlinear Optics,” In: J. M. Marulanda, Ed., *Carbon Nanotubes Applications on Electron Devices*, InTech, 2011.
- [13] Vl. A. Margulis and T. A. Sizikova, “Theoretical study of third-order nonlinear optical response of semiconductor carbon nanotubes,” *Physica B: Condensed Matter*, vol. 245, no. 2, pp. 173–189, Mar.1998.
- [14] E. Turek, T. Shiraki, T. Shiraishi, T. Shiga, T. Fujigaya, and D. Janas, “Single-step isolation of carbon nanotubes with narrow-band light emission characteristics,” *Sci Rep*, vol. 9, no. 1, p. 535, Dec. 2019

Chapter 3

Liquid-Filled HCPCF

3.1 Filling Methods

Fibers were cut to between 6cm and 8cm in length. To ensure consistent coupling and positioning, light was coupled to the core of the fiber by connecting to a solid-core PM780HP fiber via a mechanical splicing chip [2]. We replaced the air in 1550nm HCPCF with deionized water and heavy water by utilizing capillary action. To selectively fill the core of 800nm HCPCF, the photonic crystal cladding was collapsed while leaving the hollow-core open and is similarly filled with liquid using capillary action. We collapsed the cladding by placing the HCPCF opposite of a solid-core fiber in a fusion splicer [3] and adjusting arc current duration and power to melt the cladding structure while remaining distanced enough to prevent fusion with the solid-core fiber.

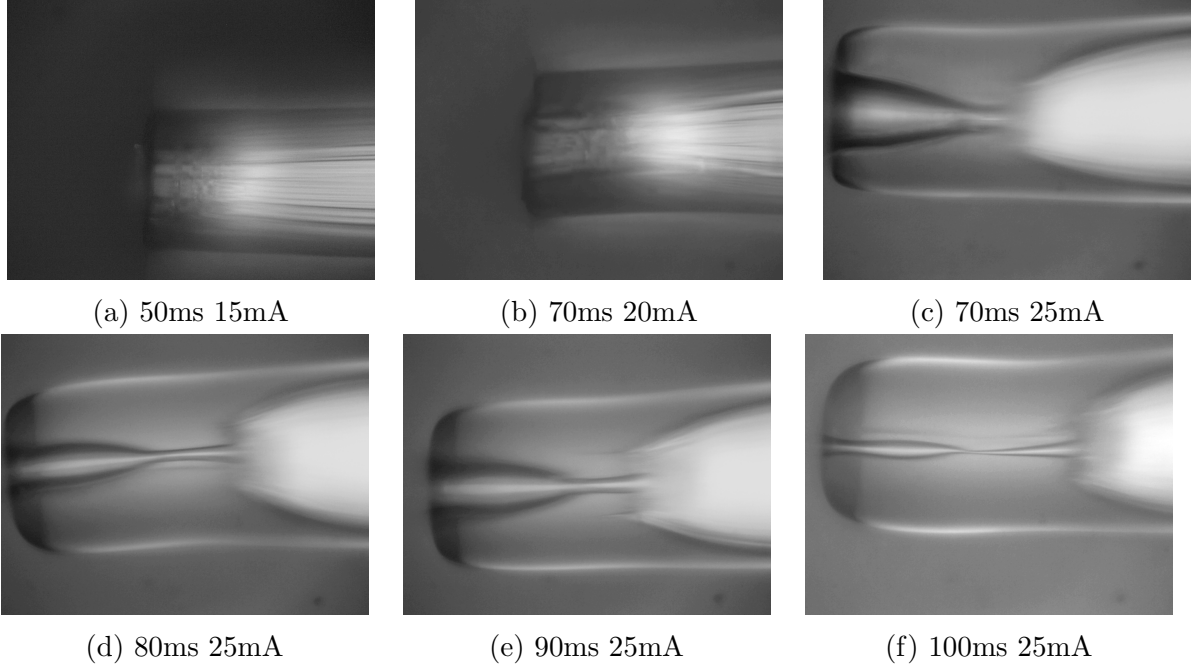


Figure 3.1: Side profile of collapsed cladding 1550HC fiber running the fiber splicer with varying current strength and duration.

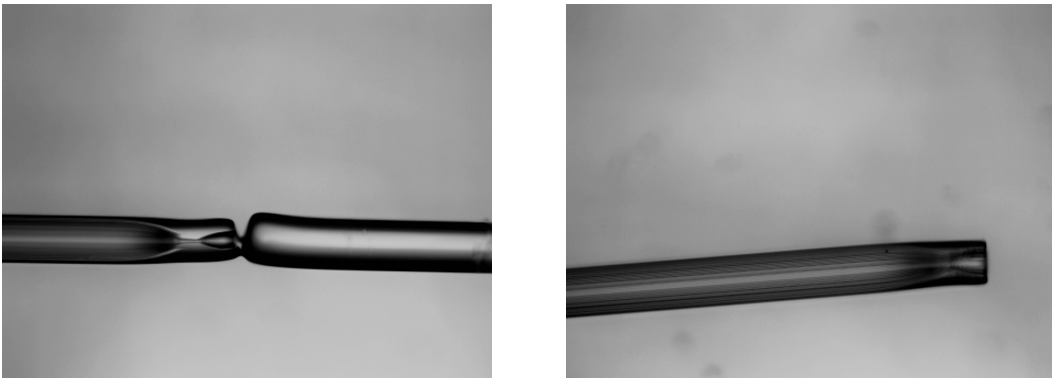


Figure 3.2: Variation between fibers using splicer settings 70ms 25ms

3.2 Experimental Set-Up

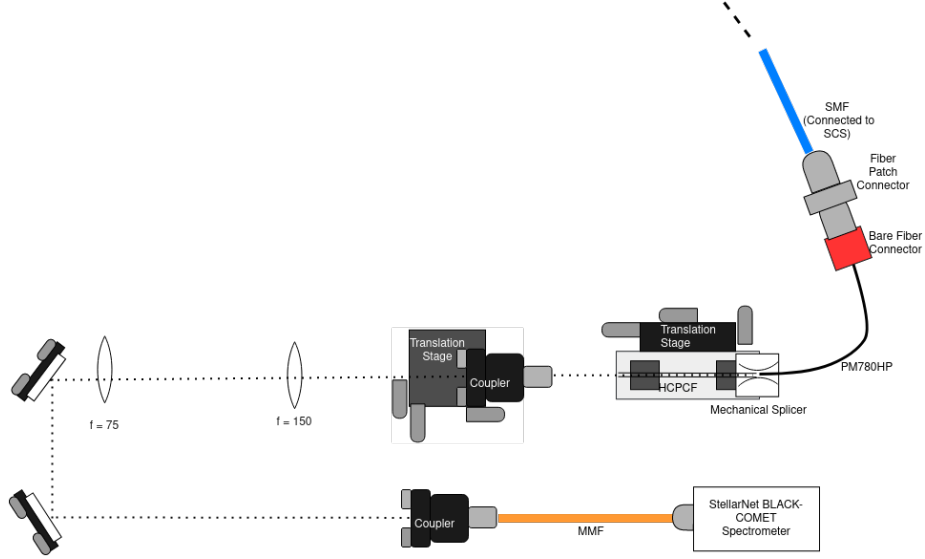


Figure 3.3: Fiber transmission experimental set-up.

3.3 H_2O and D_2O Transmission

HCPCF uses a photonic crystal cladding composed of a periodic silica structure that allows light to be guided through a hollow and thus low-refractive index core. In some applications of HCPCF, such as fiber-integrated sensors and on-linear optics, the hollow regions of the fiber are filled with liquids or gasses. Fibers that are fully-filled with water will produce a frequency shift in the bandgap due to refractive index scaling[1]. On the other hand, when the core is selectively filled with water, light will be guided via total-internal reflection. We investigate the transmission spectra of fully-filled and core-filled fibers for deionized water and heavy water.

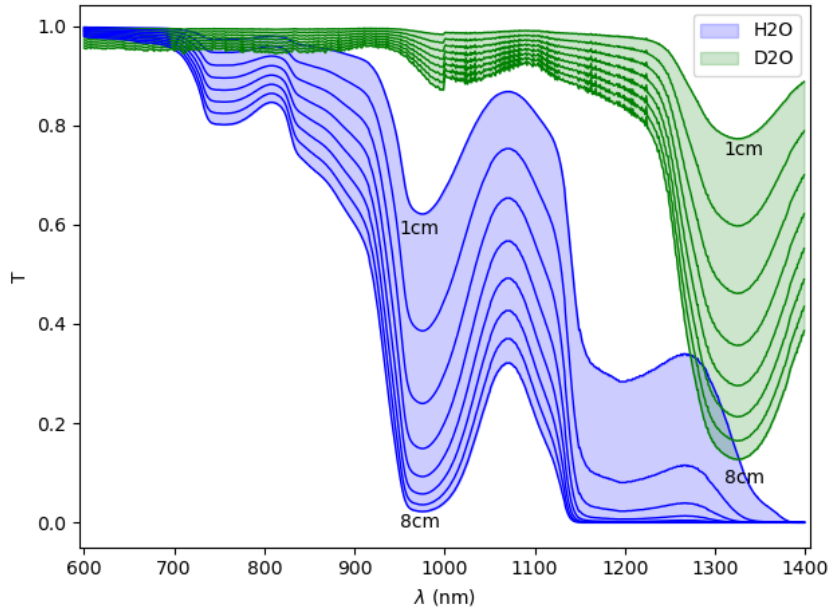


Figure 3.4: The transmission of heavy water(green) and regular water(blue) is shown for slabs of thickness ranging from 1cm to 8cm in increments of 1cm using absorption data recorded by [4].

3.4 Results

The air-filled 800nm HCPCF covers a transmission spectral range of 750nm–950nm. Light exits the fiber with a Gaussian mode shape and has an expected coupling between 75-80% when connected to a solid-core single-mode fiber. A water-filled core retains a Gaussian mode shape and has a 30% reduction in the normalized transmission for wavelengths above 850nm, which is consistent with the absorption spectrum of H₂O [4]. We also observe that the coupling efficiency of the fiber drops to 31%. With a heavy water filled core, there are no significant changes in the normalized transmission spectrum, minimal effects to the absorption over this region, and coupling efficiency of up to 67%.

The air-filled 1550nm HCPCF covers a transmission spectral range of 1200nm–1700nm. With a filled core and cladding, the spectral range shifts to transmitting wavelengths between 600nm–1100nm for both heavy water and water, which aligns with the scaling laws prediction. Heavy water achieved a coupling efficiency of 47%, but water only 16%. The existing mode shape is roughly Gaussian but contains noise as some light also leaks from the photonic structure, worse for water than heavy water. The losses seen in water are not entirely explained, but losses and effects from the decrease in refractive index contrast are also present in the D₂O-filled fiber. While there is a less than 20% difference in absorption coefficient between the 550nm–830nm for the fiber length, 7.6nm, between 830nm–950nm the absorption coefficient of water increases steeply but stays constant over the same region for heavy water.

3.4.1 Selective Filling

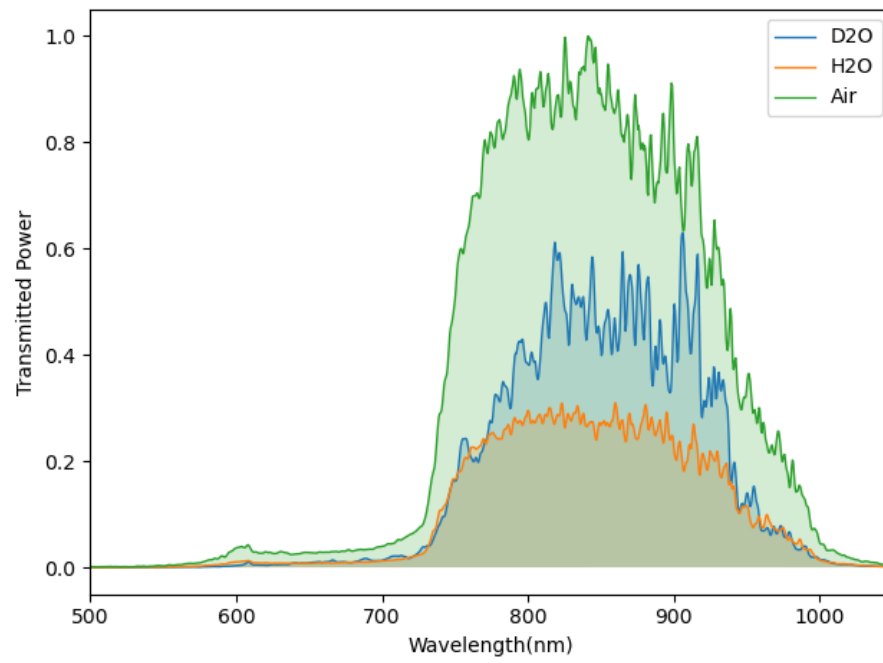


Figure 3.5: Transmission of H₂O and D₂O in (a)selectively-filled 800nm hollow-core fiber.

3.4.2 Full-Fiber Filling

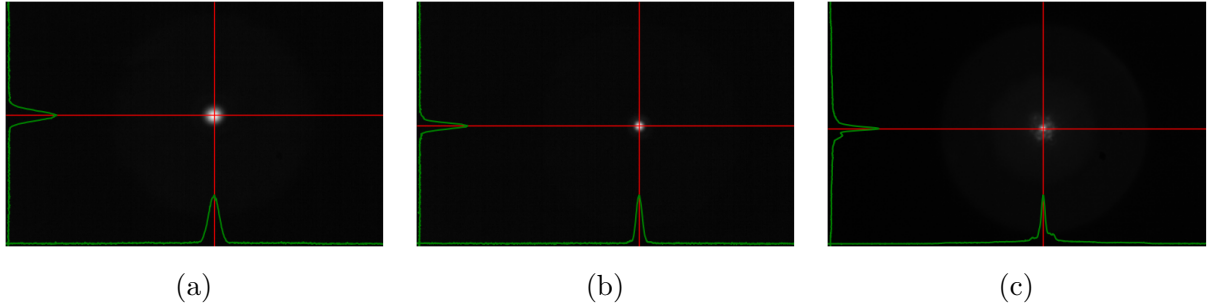


Figure 3.6: Modeshape of 1550 hollow-core fiber filled with (a)air (b)heavy water (c)distilled water. Fiber filled with heavy water maintains a Gaussian profile while the fiber with regular distilled water shows some distortion.

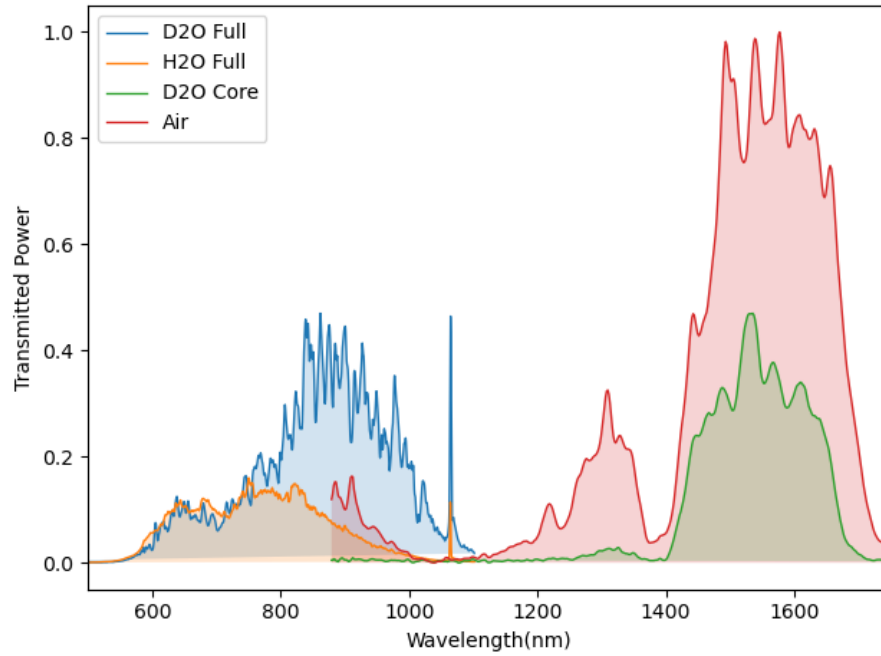


Figure 3.7: Transmission of H_2O and D_2O in fully-filled 1550nm hollow-core fiber.

Bibliography

- [1] G. Antonopoulos, F. Benabid, T. A. Birks, D. M. Bird, J. C. Knight, and P. St. J. Russell, “Experimental demonstration of the frequency shift of bandgaps in photonic crystal fibers due to refractive index scaling,” *Opt. Express*, vol. 14, no. 7, p. 3000, 2006.
- [2] R. A. Maruf and M. Bajcsy, “On-chip splicer for coupling light between photonic crystal and solid-core fibers,” *Appl. Opt.*, vol. 56, no. 16, p. 4680, Jun. 2017.
- [3] L. Xiao, W. Jin, M. S. Demokan, H. L. Ho, Y. L. Hoo, and C. Zhao, “Fabrication of selective injection microstructured optical fibers with a conventional fusion splicer,” *Opt. Express*, vol. 13, no. 22, p. 9014, 2005.
- [4] S. Kedenburg, M. Vieweg, T. Gissibl, and H. Giessen, “Linear refractive index and absorption measurements of nonlinear optical liquids in the visible and near-infrared spectral region,” *Opt. Mater. Express*, vol. 2, no. 11, p. 1588, Nov. 201.

Chapter 4

Fluorescence Tests

4.1 Bandgap Overlap

Table shows all hollow-core fiber types available from ThorLabs and the central operating wavelengths for air-filled and D2O-filled fibers. The “air” range can be used for fibers that are selectively core-filled with D2O. The ranges for HC1550 and HC800B are approximated from spectrum measurements and HC2000 and HC1060 are taken from ThorLabs datasheets. The D2O central wavelengths are calculated using the band-gap shift equation

HCPCF	λ_{AIR} (nm)	λ_{D_2O} (nm)	Range (nm)
HC2000	2000	1144	250
HC1550	1550	887	500
HC1060	1060	606	100
HC800B	800	457	200

Table 4.1: Thorlabs fiber bandgap shift.

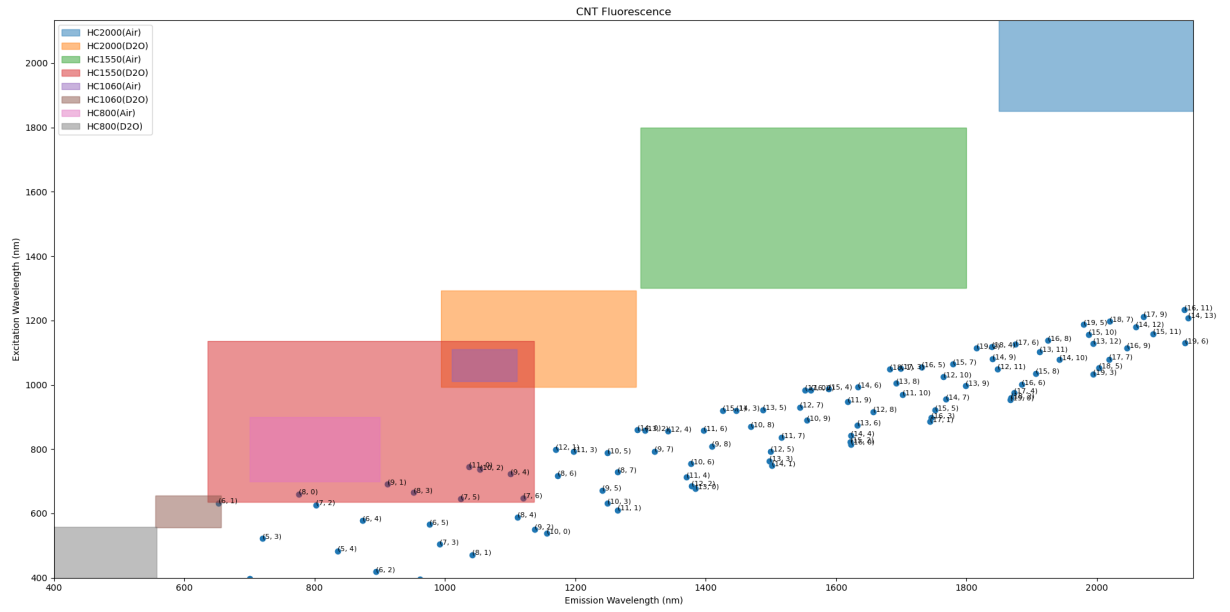


Figure 4.1: Hollow-core fiber bandgap overlayed on CNT emission vs. excitation wavelengths

(n, m)	dt (nm)	Θ (deg)	λ_{11} (nm)	λ_{22} (nm)
(6, 1)	0.52	0.13	652.62	631.79
(7, 2)	0.65	0.21	802.05	625.92
(7, 5)	0.83	0.43	1023.74	645.33
(8, 0)	0.64	0	776.01	660.25
(8, 3)	0.78	0.27	951.61	665.39
(9, 1)	0.76	0.09	912.1	691.29
(10, 2)	0.88	0.16	1053.43	736.68
(11, 0)	0.87	0	1036.93	744.57

Table 4.2: CNTs with emission and excitation transmittable through HC1550 filled with D₂O.

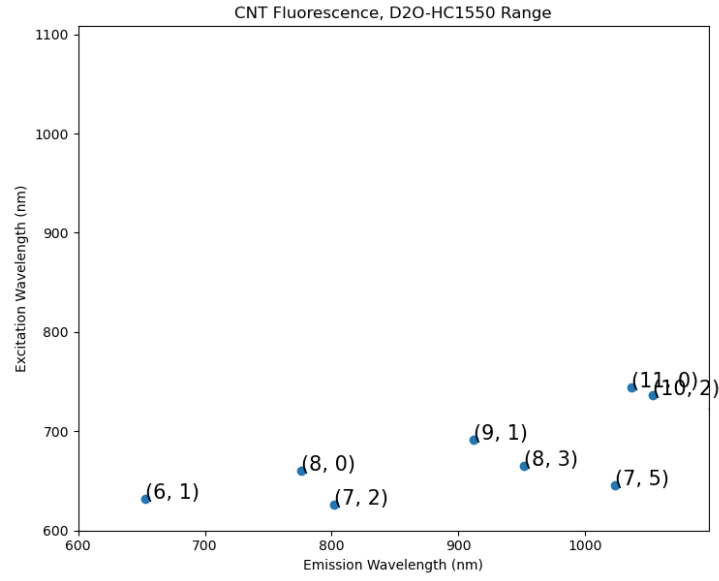


Figure 4.2: 1550HC CNTs

4.2 Indocyanine Green

Add some intro and reason for using as fake cnt

4.3 Background

4.3.1 Absorption

In [3] the absorption cross-sections of H₂O (data from [5]) and D₂O are compared at varying concentrations. The behavior in H₂O and D₂O are quite similar. However, as shown in the lower figure, for low concentrations the absorption cross-section is slightly greater for D₂O than H₂O and then slightly greater for H₂O than D₂O for high concentrations.

The absorption center wavelength also changes with concentration. From the top figure of ICG dissolved in D₂O, the low concentrations show an absorption center peak at 778nm. The distribution slowly turns dimeric at concentrations near 38.75mg/L, with a second peak popping up around 695nm. Increasing concentrations will turn the distribution monomeric again, centered at the 695nm absorption peak, reaching a maximum at a concentration near 77.5mg/L and then dimming at increasing concentrations of the solution from here.

ICG is a "J-aggregate", which is a category of dyes that have a shift in absorption band to larger wavelengths in certain solvents. ICG when mixed into water and other solvents shifts to a center wavelength of 893nm over time and can be accelerated under high heat. absorption cross-section model

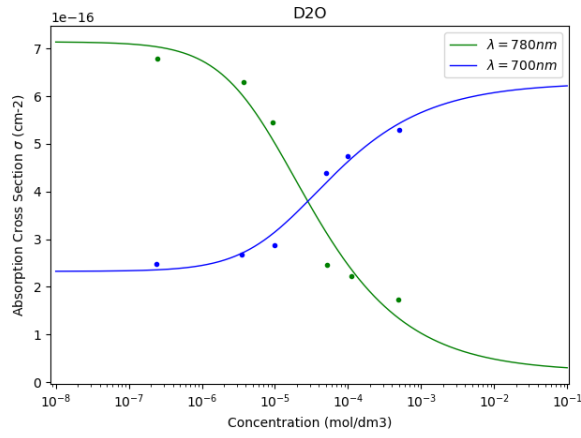
$$\sigma = x_M \sigma_M + x_D \sigma_D = \sigma_M - x_D (\sigma_M - \sigma_D) \quad (4.1)$$

dimmerization constant

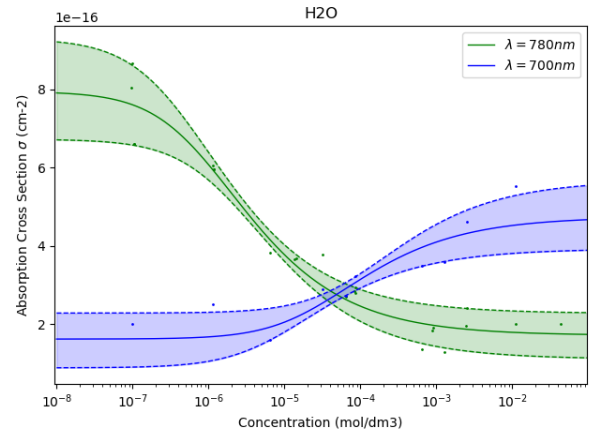
$$K_D = \frac{x_D}{2(1 - x_D)^2 C} \quad (4.2)$$

mole fraction

$$x_D = 1 + \frac{1}{4K_D C} - \sqrt{\left(1 + \frac{1}{4K_D C}\right)^2 - 1} \quad (4.3)$$



(a)



(b)

Figure 4.3: Absorption cross-section at peak wavelengths 700nm(blue) and 780nm(green) for ICG dissolved in D₂O(a) and H₂O(b) . Data from (cite) was fitted using a linear regression model.

$\lambda_{peak} = 780nm$	K_D	σ_M	σ_D
[1]	$6.01x10^5$	$9.29x10^{-16}$	$2.28x10^{-16}$
[2]	$1.03x10^5$	$6.74x10^{-16}$	$1.54x10^{-16}$
[3]	$1.40x10^5$	$6.72x10^{-16}$	$1.11x10^{-16}$
Average	$3.06x10^6$	$7.94x10^{-16}$	$1.72x10^{-16}$

Table 4.3: Absorption Cross Section parameter fitting of ICG dissolved in deionized water. Fitting done with linear regression on σ vs. concentration data measured at $\lambda = 780nm$ from literature.

$\lambda_{peak} = 700nm$	K_D	σ_M	σ_D
[1]	$3.00x10^3$	$2.29x10^{-16}$	$25.68x10^{-16}$
[3]	$3.06x10^4$	$8.89x10^{-16}$	$3.93x10^{-16}$
Average	$9.31x10^3$	$1.62x10^{-16}$	$4.74x10^{-16}$

Table 4.4: Absorption Cross Section parameter fitting of ICG dissolved in deionized water. Fitting done with linear regression on σ vs. concentration data at $\lambda = 700nm$ from literature.

λ_{peak}	K_D	σ_M	σ_D
780nm	$3.22x10^4$	$7.14x10^{-16}$	$2.68x10^{-17}$
700nm	$1.67x10^4$	$2.833x10^{-16}$	$6.28x10^{-16}$

Table 4.5: Absorption Cross Section parameter fitting of ICG dissolved in heavy water. Fitting done with linear regression on σ vs. concentration data at $\lambda = 700nm$ from literature.

4.3.2 Fluorescence

Fluorescence of J-aggregate ICG The fluorescence quantum distribution data from [5] shows that the distribution area decreases as the solution concentration increases. The absorption cross-section data from [5] is shown in the center figure for reference, though the fluorescence and absorption cross-sections were not recorded using the same sample concentrations. The fluorescence peak is around 805nm for concentrations with a 780nm absorption peak and around 810nm for concentrations with a 695nm absorption peak. The fluorescence peak begins to shift at high concentrations when the absorption cross-section begins to turn dimeric after the shift to the 695nm absorption peak.

The dimerization effects are attributed to: (1) The formation of weakly fluorescent ICG molecular aggregates at high concentrations (2) self-quenching (3) reabsorption of the emitted fluorescence by the ICG molecules due to overlap of the absorption and emission

spectra.

The maximum fluorescence intensity in water is investigated in [6] and is achieved with a ICG concentration of 2mg/L, as shown in the bottom plot.

Preparation of J-aggregate ICG from [4]: "The J-aggregates were formed by preparing a 1.5e-3M (1g/L) aqueous solution of ICG-NaI and heating it to 65 °C for a period of 32 h. The solution was then stored at room temperature. The J aggregates formed are very stable. They remain unchanged over several months. Before fluorescence measurements, the samples were diluted to a concentration of $3e - 5 \text{ mol/dm}^{-3}$ (27.12mg/L). At this concentration, the J aggregates formed remain stable over about 1 day before they detach to monomers, dimers and small oligomers.."

From [4], plotted on the right is the absorption cross-section and fluorescence quantum distribution of J-aggregate ICG in water. There is no Stokes shift between the emission and absorption peak, but notably the excitation wavelength is at 834nm and the emission peak was measured to be 890nm.

While it is possible to measure the fluorescence of the J-aggregate solution, the quantum yield is very low (roughly 3e-4) and strong light scattering does not lend to accurate measurements.

4.3.3 Photostability

The starting concentration and based on the data previously seen from [1] and [2] indicate that varying the concentration, ICG condition, and solvent will affect the storage life of the ICG solution. A table comparing these variables from [2] is included below.

Data on the time it takes a certain concentration of freshly prepared ICG solution in water and heavy water to reach half of its initial fluorescence would be extremely valuable but does not exist.

Data from [6](top right plot) compares two concentrations, 0.4mg/L and 1mg/L ICG in water. Measurements over time indicate that lower concentrations deteriorate at faster rates but will do so linearly based on the initial concentration of ICG. This is corroborated by [1](center right plot) in where the optical density of ICG in water is plotted against different dilutions made from a single stock solution. Initial measurements indicated by the circles. The stock solution was then left out for 4hrs in daylight and then prepared and measured at the same dilutions, indicated by the crosses in the plot.

Light exposure of the solution will also exasperate the degradation process, as seen in the lower right plot from [6]. Fresh ICG solution at a concentration of 1mg/L at room temperature (22C) kept in the dark and room light. The results indicate that light exposure increases the rate of which the % remaining fluorescence reduces with time.

For high-concentration ICG solutions J-aggregate solutions are stable. Solutions are typi-

cally heat-treated, like done in [4], and can be stored at room temperature for long periods.

Bibliography

- [1] W. Holzer et al., "Photostability and thermal stability of indocyanine green," *Journal of Photochemistry and Photobiology B: Biology*, vol. 47, no. 2-3, pp. 155-164, Dec. 1998.
- [2] M. L. Landsman, G. Kwant, G. A. Mook, and W. G. Zijlstra, "Light-absorbing properties, stability, and spectral stabilization of indocyanine green," *Journal of Applied Physiology*, vol. 40, no. 4, pp. 575-583, Apr. 1976.
- [3] M. Mauerer, A. Penzkofer, and J. Zweck, "Dimerization, J-aggregation and J-disaggregation dynamics of indocyanine green in heavy water," *Journal of Photochemistry and Photobiology B: Biology*, vol. 47, no. 1, pp. 68-73, Nov. 1998.
- [4] F. Rotermund, R. Weigand, W. Holzer, M. Wittmann, and A. Penzkofer, "Fluorescence spectroscopic analysis of indocyanine green J aggregates in water," *Journal of Photochemistry and Photobiology A: Chemistry*, vol. 110, no. 1, pp. 75-78, Oct. 1997.
- [5] R. Philip, A. Penzkofer, W. Bäuml, R. M. Szeimies, and C. Abels, "Absorption and fluorescence spectroscopic investigation of indocyanine green," *Journal of Photochemistry and Photobiology A: Chemistry*, vol. 96, no. 1-3, pp. 137-148, May 1996.
- [6] V. Saxena, M. Sadoqi, and J. Shao, "Degradation Kinetics of Indocyanine Green in Aqueous Solution," *Journal of Pharmaceutical Sciences*, vol. 92, no. 10, pp. 2090-2097, Oct. 2003.

4.4 Experiment Set-Up

Preparation 1. Stock 1) Using the micropipette, measure 1ml of D2O or H2O into a vial 2) Using the scale, measure 1mg of ICG powder 3) Pour the measured ICG into the 1ml of D2O/H2O 4) Close the vial and shake for 15 seconds to dissolve

2. Dilution 1) Measure 5ml of D₂O or H₂O into a vial 2) Using the pipette, measure 10ul of the stock solution 3) Output the 10ul of stock solutions into the 100ml of D₂O/H₂O 4) Close the vial and shake for 15 seconds to dissolve Used within 12 hrs of creation

4.5 Results

Chapter 5

Future Work

5.1 ECDL

References

APPENDICES

Appendix A

Bragg Gratings

A.1 Derivation of the 1D Propagation Matrix

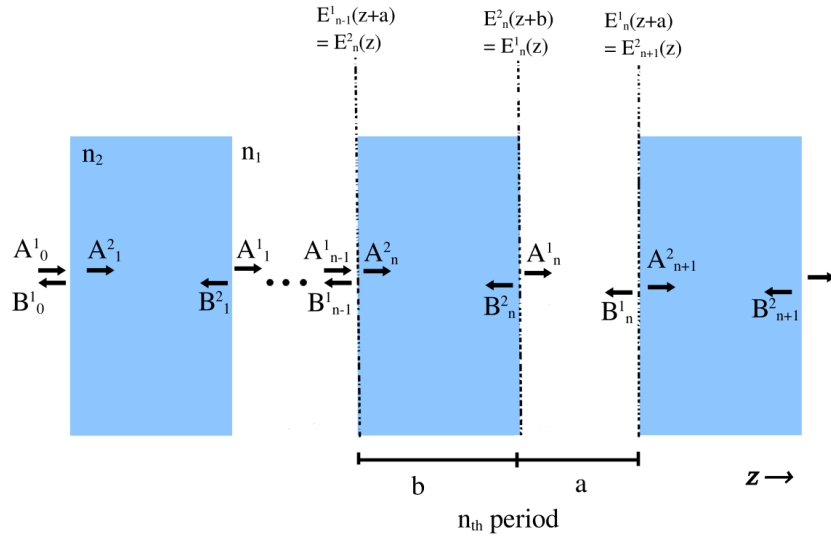


Figure A.1: Schematic of quarter wavelength stack

$$\begin{aligned} E_n^1(z) &= A_n^1 e^{-ik_{z1}(z-(n-1)a)} + B_n^1 e^{ik_{z1}(z-(n-1)a)}; (n-1)a + b < z < na \\ E_n^2(z) &= A_n^2 e^{-ik_{z2}(z-(n-1)a)} + B_n^2 e^{ik_{z2}(z-(n-1)a)}; (n-1)a < z < (n-1)a + b \end{aligned} \quad (\text{A.1})$$

Where $k_j = \frac{2\pi}{n_j}$ The boundary conditions:

continuous between the layers:

$$E_n^1(z) = E_n^2(z + b) \quad (\text{A.2})$$

The second condition is that the electric field is smooth, which can be established in the perpendicular magnetic field. i.e. Maxwell's equations for a monochromatic field with freq ω and time dependence $e^{-i\omega t}$

$$\begin{aligned} \vec{\nabla} \times \vec{H} &= -i\omega\epsilon(\vec{r})\vec{E} \\ \vec{\nabla} \times \vec{E} &= i\omega\mu_0\vec{H} \end{aligned} \quad (\text{A.3})$$

Assuming that the electric field is linearly polarized $E(z) = \hat{x}E(z)$, then the magnetic field (via Faraday's law) $H(z) = \hat{y}H(z)$ gives the corresponding magnetic field for the two layers

$$\begin{aligned} H_n^1(z) &= \frac{1}{\eta_1} [A_n^1 e^{-ik_{z1}(z-(n-1)a)} - B_n^1 e^{ik_{z1}(z-(n-1)a)}] \\ H_n^2(z) &= \frac{1}{\eta_2} [A_n^2 e^{-ik_{z2}(z-(n-1)a)} - B_n^2 e^{ik_{z2}(z-(n-1)a)}] \end{aligned} \quad (\text{A.4})$$

$$\begin{aligned} A_n^2(z) &= \frac{1}{2} [E_n^2(z) + \eta_2 H_n^2(z)] \\ B_n^2(z) &= \frac{1}{2} [E_n^2(z) - \eta_2 H_n^2(z)] \end{aligned} \quad (\text{A.5})$$

Where the impedance $\eta_2 = \frac{\eta_0}{n_2}$

Putting these relations into a matrix form we can find a a solution for the transition boundary:

$$\begin{aligned} \begin{bmatrix} E_{n-1}^1(z+a) \\ H_{n-1}^1(z+a) \end{bmatrix} &= \begin{bmatrix} E_n^2(z) \\ H_n^2(z) \end{bmatrix} \\ \begin{bmatrix} 1 & 1 \\ \eta_1^{-1} & -\eta_1^{-1} \end{bmatrix} \begin{bmatrix} A_{n-1}^1(z+a) \\ B_{n-1}^1(z+a) \end{bmatrix} &= \begin{bmatrix} 1 & 1 \\ \eta_2^{-1} & -\eta_2^{-1} \end{bmatrix} \begin{bmatrix} A_n^2(z) \\ B_n^2(z) \end{bmatrix} \\ \begin{bmatrix} A_{n-1}^1(z+a) \\ B_{n-1}^1(z+a) \end{bmatrix} &= M_{1 \rightarrow 2} \begin{bmatrix} A_n^2(z) \\ B_n^2(z) \end{bmatrix} \\ \begin{bmatrix} A_{n-1}^1(z+a) \\ B_{n-1}^1(z+a) \end{bmatrix} &= M_{1 \rightarrow 2} \begin{bmatrix} A_n^2(z) \\ B_n^2(z) \end{bmatrix} \end{aligned} \quad (\text{A.6})$$

The transition matrix:

$$M_{1 \rightarrow 2} = \frac{1}{2} \begin{bmatrix} 1 + \frac{k_2}{k_1} & 1 - \frac{k_2}{k_1} \\ 1 - \frac{k_2}{k_1} & 1 + \frac{k_2}{k_1} \end{bmatrix} \quad (\text{A.7})$$

The plane wave propagating though the material will acquire a phase:

$$M_{n_2} = \begin{bmatrix} e^{ik_{z2}b} & 0 \\ 0 & e^{-ik_{z2}b} \end{bmatrix} \quad (\text{A.8})$$

Thus the travel through the n2 material can be summarized by

$$\begin{bmatrix} A_{n-1}^1(z+a) \\ B_{n-1}^1(z+a) \end{bmatrix} M_{1 \rightarrow 2} M_{n2} \begin{bmatrix} A_n^2(z+b) \\ B_n^2(z+b) \end{bmatrix} \quad (\text{A.9})$$

For the electric field through the n1 region :

$$M_{1 \rightarrow 2} = \frac{1}{2} \begin{bmatrix} 1 + \frac{k_1}{k_2} & 1 - \frac{k_1}{k_2} \\ 1 - \frac{k_1}{k_2} & 1 + \frac{k_1}{k_2} \end{bmatrix} M_{n1} = \begin{bmatrix} e^{ik_{z1}a} & 0 \\ 0 & e^{-ik_{z1}a} \end{bmatrix} \quad (\text{A.10})$$

Becomes one periodic transition matrix:

$$M_p = M_{1 \rightarrow 2} M_{n2} M_{2 \rightarrow 1} M_{n1} = \begin{bmatrix} m_{11} & m_{12} \\ m_{21} & m_{22} \end{bmatrix}$$

For an N period block:

$$\begin{bmatrix} A_0 \\ B_0 \end{bmatrix} = (M_p)^N \begin{bmatrix} A_{(N+1)} \\ 0 \end{bmatrix} \quad (\text{A.11})$$

Glossary

This document is incomplete. The external file associated with the glossary ‘main’ (which should be called `uw-ethesis.gls`) hasn’t been created.

Check the contents of the file `uw-ethesis.glo`. If it’s empty, that means you haven’t indexed any of your entries in this glossary (using commands like `\gls` or `\glsadd`) so this list can’t be generated. If the file isn’t empty, the document build process hasn’t been completed.

You may need to rerun \LaTeX . If you already have, it may be that \TeX ’s shell escape doesn’t allow you to run `makeindex`. Check the transcript file `uw-ethesis.log`. If the shell escape is disabled, try one of the following:

- Run the external (Lua) application:
`makeglossaries-lite "uw-ethesis"`
- Run the external (Perl) application:
`makeglossaries "uw-ethesis"`

Then rerun \LaTeX on this document.

This message will be removed once the problem has been fixed.

Abbreviations

This document is incomplete. The external file associated with the glossary ‘abbreviations’ (which should be called `uw-ethesis.gls-abr`) hasn’t been created.

Check the contents of the file `uw-ethesis.glo-abr`. If it’s empty, that means you haven’t indexed any of your entries in this glossary (using commands like `\gls` or `\glsadd`) so this list can’t be generated. If the file isn’t empty, the document build process hasn’t been completed.

You may need to rerun \LaTeX . If you already have, it may be that \TeX ’s shell escape doesn’t allow you to run `makeindex`. Check the transcript file `uw-ethesis.log`. If the shell escape is disabled, try one of the following:

- Run the external (Lua) application:
`makeglossaries-lite "uw-ethesis"`
- Run the external (Perl) application:
`makeglossaries "uw-ethesis"`

Then rerun \LaTeX on this document.

This message will be removed once the problem has been fixed.

Nomenclature

This document is incomplete. The external file associated with the glossary ‘nomenclature’ (which should be called `uw-ethesis.nomenclature-gls`) hasn’t been created.

Check the contents of the file `uw-ethesis.nomenclature-glo`. If it’s empty, that means you haven’t indexed any of your entries in this glossary (using commands like `\gls` or `\glsadd`) so this list can’t be generated. If the file isn’t empty, the document build process hasn’t been completed.

You may need to rerun \LaTeX . If you already have, it may be that \TeX ’s shell escape doesn’t allow you to run `makeindex`. Check the transcript file `uw-ethesis.log`. If the shell escape is disabled, try one of the following:

- Run the external (Lua) application:
`makeglossaries-lite "uw-ethesis"`
- Run the external (Perl) application:
`makeglossaries "uw-ethesis"`

Then rerun \LaTeX on this document.

This message will be removed once the problem has been fixed.

List of Symbols

This document is incomplete. The external file associated with the glossary ‘symbols’ (which should be called `uw-ethesis.symbols-gls`) hasn’t been created.

Check the contents of the file `uw-ethesis.symbols-glo`. If it’s empty, that means you haven’t indexed any of your entries in this glossary (using commands like `\gls` or `\glsadd`) so this list can’t be generated. If the file isn’t empty, the document build process hasn’t been completed.

You may need to rerun \LaTeX . If you already have, it may be that \TeX ’s shell escape doesn’t allow you to run `makeindex`. Check the transcript file `uw-ethesis.log`. If the shell escape is disabled, try one of the following:

- Run the external (Lua) application:
`makeglossaries-lite "uw-ethesis"`
- Run the external (Perl) application:
`makeglossaries "uw-ethesis"`

Then rerun \LaTeX on this document.

This message will be removed once the problem has been fixed.